Chapter 2
Three-Dimensional Centrifuge and Numerical Modeling of Underground Structures Subjected to Normal Faulting

Charles Wang Wai Ng, Qipeng Cai, and Sina Baghbanrezvan

2.1 Introduction

Earthquake-induced fault rupture propagation in overlying soil has a significant impact on underground structures adjacent to the fault. Extensive damage to pile foundation and tunnel has been recorded in recent catastrophic earthquakes such as the 1999 Chi-chi and Kocaeli earthquakes and the 2008 Wenchuan earthquake (Wang et al. 2001; Dong et al. 2003; Anastasopoulos and Gazetas 2007; Faccioli et al. 2008; Li 2008; Wang et al. 2009). Seismic codes worldwide advise against construction in the vicinity of an active fault (EAK 2000; EC8 2002; GB50011-2010 2010), but it remains a challenge to determine a reasonable distance to the free-field rupture outcrop for the safe design of a pile foundation. Meanwhile, the safe distance to the free-field rupture outcrop is generally not applicable to tunnel design in a seismically active zone because faults have a large zone of influence on tunnels. Hence, it is critical to identify the potential damage zone to protect the tunnel.

For a soil layer overlying a bedrock fault, the dip angle of the fault rupture in the soil generally varies with distance to the ground surface (Bray et al. 1994). The fault rupture path is strongly influenced by a variety of factors such as the properties of the overlying soil, the type of bedrock fault, the magnitude of bedrock fault movement and even an underground structure (Cole and Lade 1984; Loukidis 2009). When there is an underground structure, the fault rupture path may be substantially modified, and the rupture may still propagate from the bedrock to the ground surface. The interaction between fault rupture in soil and a shallow foundation has recently attracted considerable attention (Anastasopoulos et al. 2007,

C. W. W. Ng (✉) · S. Baghbanrezvan
Hong Kong University of Science and Technology Clear Water Bay, Kowloon, Hong Kong
e-mail: cecwwng@ust.hk

Q. Cai
Hua Qiao University, No. 668, Jimei Avenue, Xiamen 361021, China

T. G. Sitharam et al. (eds.), *Latest Developments in Geotechnical Earthquake Engineering and Soil Dynamics*, Springer Transactions in Civil and Environmental Engineering, https://doi.org/10.1007/978-981-16-1468-2_2

2008, 2009; Ahmed and Bransby 2009; Ashtiani et al. 2015). A heavily loaded shallow foundation may divert the rupture completely away from the structure (Anastasopoulos et al. 2007). The development of such interaction mechanisms may be even more evident for pile foundations due to the load transfer to a deeper soil layer. Because of the complex interaction mechanism between a pile foundation and fault rupture, determination of the safe distance to the free-field rupture outcrop for piles remains a major challenge (Anastasopoulos et al. 2013; Cai and Ng 2016).

Field case studies following the 2008 Wenchuan earthquake in China revealed that fault movement caused more severe damage to tunnels than did the seismic waves (Li 2008; Wang et al. 2009). The tunnel lining had been sheared off and had even collapsed due to permanent ground deformation. Several model tests have been conducted to investigate the interaction between a tunnel and fault rupture propagation in soil (Baziar et al. 2014, 2019; Kiani et al. 2016; Cai et al. 2019). These studies have illustrated the importance of the proper estimation of forces in a tunnel lining induced by faulting as well as identifying a potential damage zone for the design of tunnels.

This keynote paper consists of two major parts. In the first part, three-dimensional centrifuge model test results of a single pile and a pile group (1×3) subjected to normal fault propagation in dry Toyoura sand are reported. The single pile was located on the footwall side of the bedrock fault line. For the pile group, three piles were connected with an elevated pile cap in which one of the piles located on the footwall side with the same distance as the single pile. A numerical parametric study using a strain-softening Mohr–Coulomb model in FLAC3D was conducted to investigate the effects of the distance from the pile foundation to the free-field fault rupture outcrop on the responses of the pile foundation. In addition, the distance to the free-field fault rupture outcrop was examined for both the single pile and the pile group. In the second part of the paper, the influence of normal faulting on a tunnel in sand is investigated through a series of three-dimensional centrifuge model tests and numerical back-analyses. This keynote paper summarizes and reinterprets published data from Cai and Ng (2016), Cai et al. (2017, 2019).

2.2 Problem Definition

Figure 2.1a shows a pile foundation in soil deposits subjected to underlying normal faulting. The horizontal distance from the furthest edge of the pile cap with a width of B (or single pile with a diameter of d) to the free-field fault rupture outcrop is defined by S. The horizontal distance of the soil at the ground surface from the free-field fault rupture outcrop is defined by X. The vertical component of the magnitude and the dip angle of the bedrock fault are h and α, respectively. Figure 2.1b shows a tunnel which is also subjected to underlying normal faulting.

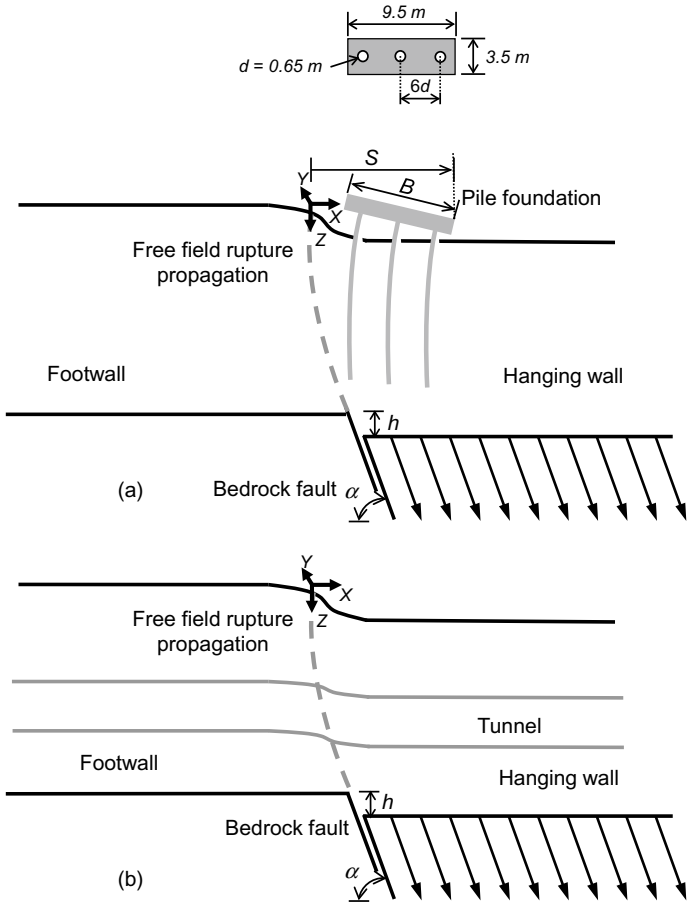

Fig. 2.1 Problem definition: interaction between fault rupture propagation and **a** pile foundation, **b** tunnel

2.3 Three-Dimensional Centrifuge and Numerical Modeling of Pile-Faulting and Tunnel-Faulting Interaction

2.3.1 Experimental Program and Setup

The centrifuge model tests reported in this keynote were conducted at the Hong Kong University of Science and Technology (HKUST). The 400 *g*-t geotechnical centrifuge at the HKUST is equipped with advanced simulation capabilities including the world's first in-flight biaxial (2D) shaker (Ng et al. 2004), an advanced four-axis robotic manipulator and a state-of-the-art data acquisition and

Table 2.1 Scaling laws relevant to centrifuge modeling

Quantity	Scaling law (model/prototype)
Length	$1/N$
Displacement	$1/N$
Stress	1
Strain	1
Density	1
Force	$1/N^2$
Bending moment	$1/N^3$
Axial rigidity (EA)	$1/N^2$
Flexural stiffness (EI)	$1/N^4$

control system (Ng et al. 2001; Ng et al. 2002; Ng 2014). This beam centrifuge with a diameter of 8.4 m is equipped with two swinging platforms, one for static tests and one for dynamic tests. All the tests reported in this paper were performed with an effective centrifugal acceleration of 50 g. The scaling laws relevant to this study are summarized in Table 2.1 (Taylor 1995).

Figure 2.2a shows the schematic diagram of the centrifuge model setup with a single pile in test SP. The dimensions of the model container were 350 × 1170 400 mm (width × length × height) in model scale. The shaft length and the distance to the bedrock fault line of the model pile were 300 mm and 91 mm, respectively. Thus, the single pile is located on the footwall. To form the 3 × 1 pile group (for test PG), two more piles were installed on the hanging wall side of the single pile (refer to Fig. 2.1a for details).

Figure 2.2b shows a schematic elevation view of the model container with a tunnel in test *U*. The sand layer was 500 mm thick and the tunnel crown was located 100 mm below the model surface. For the other test (test *M*), the tunnel crown was located 200 mm below the model surface. The hydraulic cylinder and the hanging wall base were installed at the bottom of the strongbox to simulate normal faulting. Driven by a hydraulic cylinder, the hanging wall block could move along a target direction at an angle of 70° with respect to the horizontal (Ng et al. 2012; Cai et al. 2013; Cai and Ng 2014). More details of the hydraulic cylinder and the unconstrained boundary container are given later in the paper.

2.3.2 Model Pile and Model Tunnel

Figure 2.3a shows a schematic elevation view of the single pile. The model piles were made from hollow square aluminum tubes with a width of 10.0 mm and a thickness of 0.7 mm. The pile shaft was coated with a layer of epoxy 1.5 mm in thickness to protect the attached strain gauge and to provide a uniform pile–soil interface (Ng et al. 2013, 2014, 2015, 2017; Ng and Lu 2014). The final width of the square section of the model pile was 13 m (0.65 m in prototype when tested at

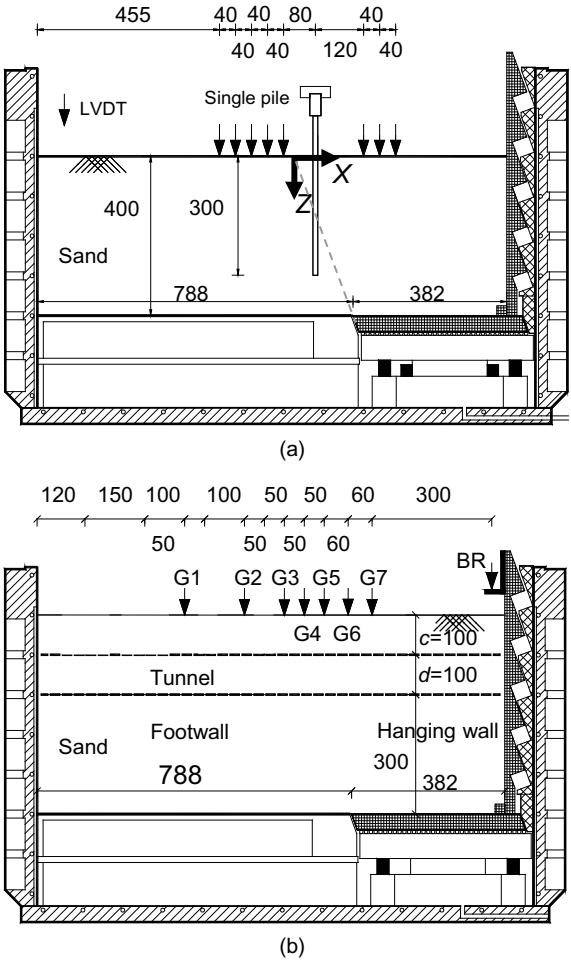

Fig. 2.2 Cross-section of the experimental apparatus for: **a** the single pile test; and **b** the tunnel test

50 g). For the 3 × 1 pile group, three single piles were firmly fixed to a relatively rigid pile cap with a center-to-center spacing of 78 mm (3.90 m in prototype) (see Fig. 2.3b). The pile cap was elevated by 155 mm (7.75 m in prototype) and so the embedded depth of each pile was 300 mm (15.00 m in prototype). Given Young's modulus of aluminum alloy (=70 GPa) and the epoxy coating (=2 GPa), the bending stiffness of the model pile was 75.3 kN m^2 in model scale (4.71 × 108 kN m^2 in prototype).

Figure 2.3c shows a schematic elevation view of the model tunnel. The model tunnel was made from an aluminum alloy tube. The outer diameter (D) and the lining thickness were 100 and 3 mm, respectively, equivalent to 5,000 and 150 mm in prototype scale when tested at 50 g. The model tunnel was 1,150 mm long, equivalent to 57.5 m in prototype. The scaling law for the flexural stiffness of the whole model tunnel is $1/N^4$. By assuming Young's modulus (E_c) of 33 GPa (ACI

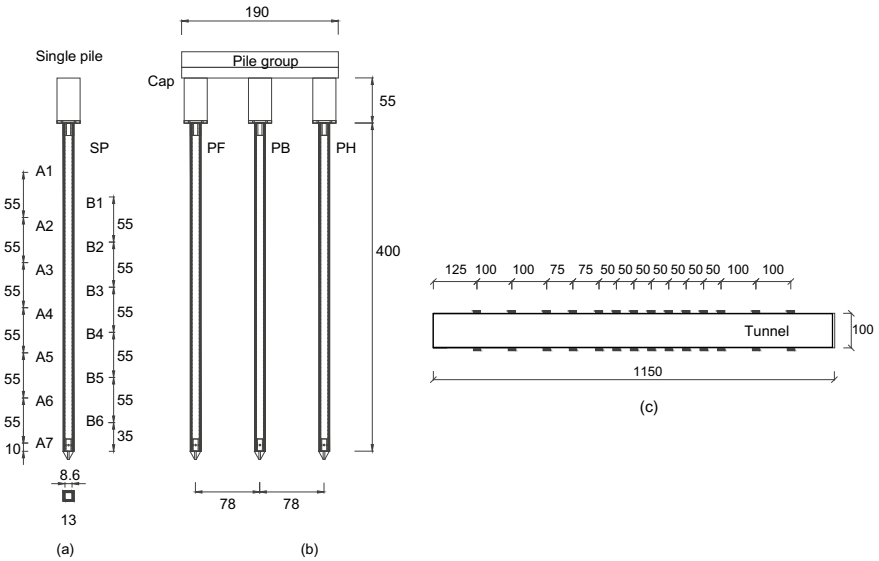

Fig. 2.3 **a** Model single pile; **b** model pile group; and **c** model tunnel (dimensions in mm)

2011), the tunnel lining thickness is equivalent to 360 mm in prototype scale in the longitudinal direction of the tunnel. The two ends of the tunnel were not connected to the model box and no additional fixity was imposed.

2.3.3 Model Preparation

For simplicity, dry Toyoura sand was used in all the tests reported. Toyoura sand is a uniform fine sand having a mean grain size (D_{50}) of 0.17 mm, a maximum void ratio of 0.977, a minimum void ratio of 0.597, a specific gravity of 2.65 and an angle of friction at the critical state ϕ'_{cv} of 31° (Ishihara 1993).

Figure 2.4 shows the prepared model package for the centrifuge tests. The pluvial deposition method was adopted to prepare all the centrifuge models. Dry Toyoura sand was rained onto the base of the model box from a height of 500 mm above the sand bed to give a medium-dense sand layer (with a relative density of 62–65%). For tests on the pile foundation (test SP and test PG), once the surface of the sand bed had reached the level where the pile toe should be, the pile was temporarily fixed in position before the sand deposition process was resumed. For tests on the tunnel (test *U* and test *M*), the model tunnel was laid flat on the sand bed once the surface of the sand bed had reached the level where the invert of the tunnel should be.

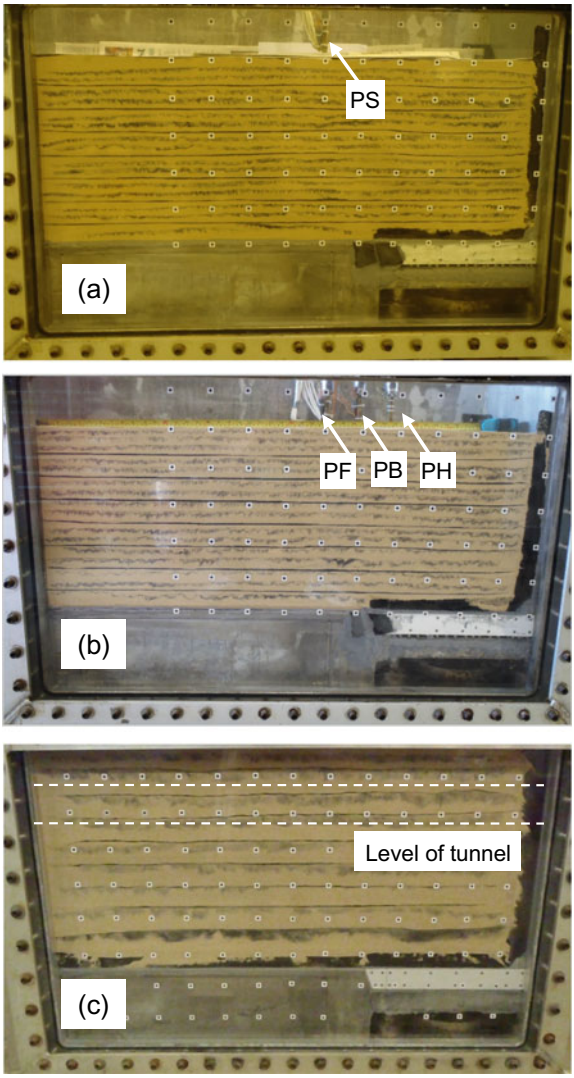

Fig. 2.4 Model package before the centrifuge test on **a** the single pile (test SP); **b** the pile group (test PG); and **c** the tunnel (test *U*)

2.3.4 Instrumentation and Centrifuge Model Test Procedure

After each model preparation, the model package was transferred to the centrifuge platform. Typical instrumentation layouts for the tests on the single pile (test SP) and the tunnel (test *U*) are shown in Fig. 2.2a, b, respectively. Linear variable differential transformers (LVDTs) were mounted on the model surface and at the top of the boundary wall on the hanging wall side to measure settlements of the ground surface and the bedrock hanging wall. Four digital cameras were installed to

record soil deformation during faulting in-flight. The digital images were then analyzed using the Geo-PIV program developed by White et al. (2003).

A vertical load of 0.5 kN (1,250 kN in prototype when tested at 50 g) was applied to the pile top in the single pile test and each individual pile in the elevated pile group. The working load was chosen based on the ultimate capacity of the prototype pile, which was 0.81 kN (2,036 kN in prototype) estimated as a summation of shaft resistance and end bearing capacity. The centrifuge was then spun up to 50 g and reached a steady state. Subsequently, normal fault movement was simulated by a downward movement of the hanging wall block in five steps of h = 8 mm, 16 mm, 26 mm, 36 mm and 42 mm (i.e., h = 0.4 m, 0.8 m, 1.3 m, 1.8 m and 2.1 m in prototype) Fig. 2.5 shows a cross section of the model container and the hydraulic actuator used to control the downward fault movement together with the unconstrained boundary. The effects of using a constrained and unconstrained boundary were reported by Cai et al. (2015).

The fault movement was controlled by draining off the oil in the hydraulic cylinder resulting in the downward movement of the platen. The vertical settlement of the platen was controlled by four platen guides around the cylinder. After spinning down the centrifuge, post-experiment observations were made and the failure patterns on the model surfaces were recorded.

For the tunnel tests, the centrifuge was spun up to an acceleration of 50 g and sufficient time was allowed for the transducers to stabilize. Subsequently, normal faulting was simulated in-flight with a fault movement of h = 16 mm (i.e., 0.8 m in prototype). After applying a normal fault movement, a sufficient time lapse was allowed until readings of transducers became stable. Ground surface settlement and the induced axial strains were measured during the normal faulting.

2.3.5 *Numerical Back-Analysis of Centrifuge Tests*

A series of three-dimensional finite-difference analyses were performed using FLAC3D to examine the interaction between an underground structure and faulting.

Figure 2.6a shows a typical numerical mesh for analyzing the failure of a single pile induced by normal faulting in the SP test. The mesh and pile configuration had the same dimensions in the numerical run as in the centrifuge test. The boundary conditions adopted in the finite-difference analysis were roller-support on the four vertical sides and pin-support at the base of the mesh. The soil was modeled using four-node tetrahedral elements. The pile was modeled by a 'pile' element in FLAC3D (Itasca 2000).

Dry Toyoura sand with a density of 1533 kg/m^3 was described using an elastoplastic constitutive model with a strain-softening Mohr–Coulomb failure criterion. The peak friction angle (ϕ_{peak}), critical-state friction angle (ϕ_c), dilation angle (ψ), elasticity modulus (E) and Poisson ratio (υ) of the sand were taken to be 38°, 31°, 10°, 36 MPa and 0.2, respectively (Cai et al. 2019). The post-peak

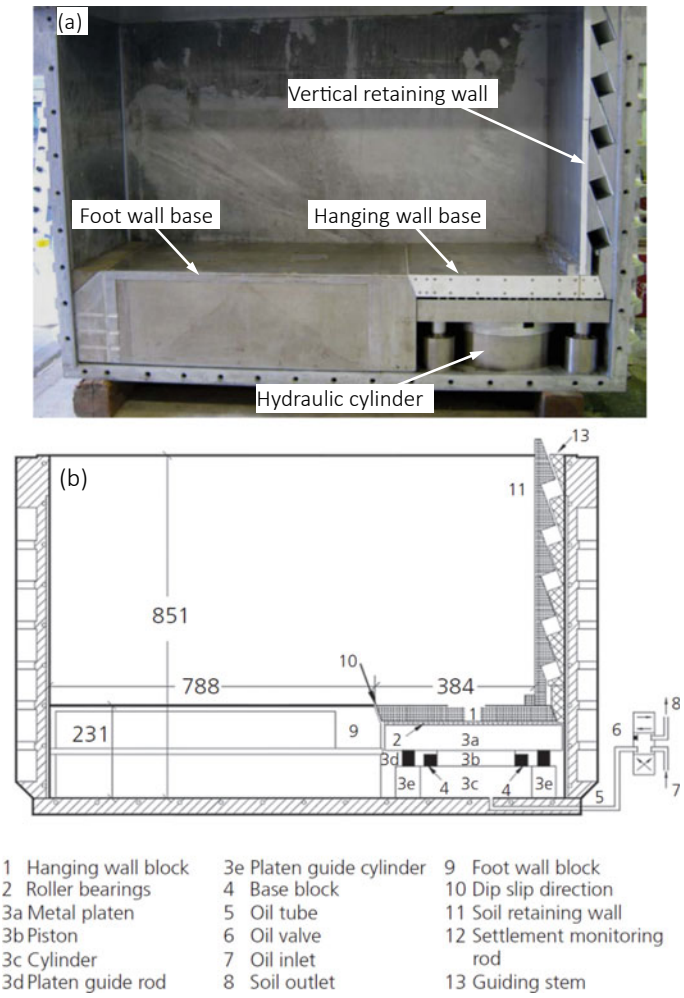

Fig. 2.5 Cross section of the container for centrifuge tests: **a** hydraulic cylinder for simulation of normal fault movement and **b** unconstrained boundaries (all dimensions in mm)

strain-softening behavior of the soil was modeled by a linear reduction in the friction angle with the accumulated plastic strain. This modeling technique has been deemed suitable for simulating fault rupture propagation (Anastasopoulos et al. 2007; Ng et al. 2012; Cai and Ng 2014; Cai et al. 2019).

The model pile was modeled as a linear elastic material with Young's modulus of 70 GPa and Poisson ratio of 0.2. The pile–soil interface was modeled as a spring-slider system (Itasca 2000). Stiffness in the normal direction (k_n) and that in the shear direction (k_s) were both estimated by

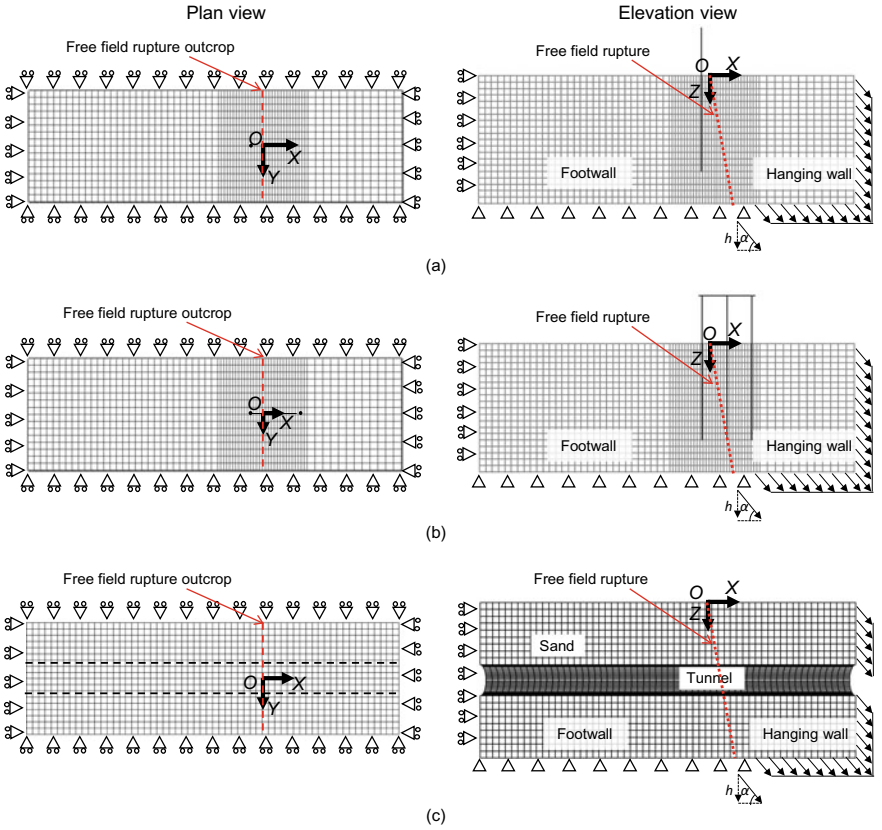

Fig. 2.6 Meshes and boundary conditions for numerical analysis of **a** the single pile; **b** the pile group; and **c** the tunnel

$$\max\left[\frac{(K+3G/4)}{\Delta z_{\min}}\right] \tag{2.1}$$

where K is the bulk modulus; G is the shear modulus; and $\Delta z_{\min}$ is the smallest dimension of an adjoining zone in the normal direction. Since $\Delta z_{\min}$ = 2 mm in this study, k_n and k_s were both taken to be 1.75 $\times$ 10^7 kPa/m. The friction angle of the pile–soil interface (ϕ_s) was taken to be the critical-state friction angle of the surrounding soil ($\phi_c = 31^\circ$).

In each numerical analysis, prior to the simulation of bedrock fault movement, model dimensions were used but the gravity was increased to 50 g to obtain the same initial in situ stresses as those in the centrifuge. Inclined downward displacements were then applied at the grid points along the vertical side and the base

of the soil mesh on the hanging wall side to simulate normal faulting. The grid point displacements of the soil were the same as those of the bedrock fault in centrifuge tests.

Figure 2.6a, b shows the numerical mesh of single pile and pile group subjected to normal faulting, respectively. The single pile and pile group configurations in the numerical analysis were identical to that in the centrifuge tests. To simplify the analysis, the pile cap was also simulated by a 'pile' element. Each pile top was fixed to the pile cap and a total vertical loading of 1.5 kN (3750 kN in prototype) was applied to the pile cap.

Figure 2.6c shows the numerical mesh for analyzing the response of the tunnel subjected to normal faulting (test *M*). The tunnel was modeled by 'liner' elements. The mesh of the tunnel lining had the same distribution as the adjacent grids of the soil. To investigate the stiffening effects provided by the tunnel, three different tunnel stiffness were adopted in numerical simulation, in which Young's modulus of the tunnel (E_T) was reduced to 0.65 E_T and 0.17 E_T (Cai et al. 2019). The friction angle between the tunnel lining and the surrounding soil was taken to be 20° (i.e., two-thirds of the critical-state friction angle of soil). Since model dimensions were used, an enhanced gravity of 50 g was also applied in numerical simulations. This was followed by applying an inclined downward displacement at the grid points along the vertical side and the base of the soil mesh on the hanging wall side to simulate normal faulting. No displacement was imposed on the two ends of the tunnel to simulate the free boundary condition adopted in the centrifuge test. Numerical back-analysis of the centrifuge test *U* was also conducted.

2.3.6 *Parametric Study of Pile-Fault-Distance and Tunnel Depth*

To investigate the effects of pile-fault-distance on the responses of a single pile and a pile group, a series of numerical analyses were conducted by varying the horizontal distance (*S*) (see Fig. 2.1) from the pile or pile group edge to the free-field fault outcrop, as summarized in Table 2.2. The performance of the single pile and pile group was further evaluated in terms of pile displacements, redistribution of axial forces and the induced bending moments.

Table 2.2 Summary of the numerical analysis of pile-fault interaction

Series	Description	Distance of pile face or pile cap edge to free-field fault outcrop '*S*' (m) (refer to Fig. 2.1)
1	Single pile	−21.2, −16.2, −12.2, −6.2, −2.5, −0.5, 3.5, 9.5, 15.5, 21.5, 28.5
2	Pile group	−15.5, −15.0, −14.5, −14.0, −13.5, −13.0, −12.5, −12.0, −10.5, −8.5, −6.5, −4.5, −2.5, −0.5, 1.5, 3.5, 5.5, 7.5, 9.5, 11.5, 13.5, 15.5, 17.5, 19.5, 21.5, 23.5, 25.5, 27.5, 29.5, 31.5

Table 2.3 Summary of the numerical analysis plan of tunnel-fault interaction

Series	Description	Young's modulus of tunnel (GPa)	Tunnel depth d_T (m)
1	Back analyses of centrifuge tests	70	7.5, 12.5
2	Effects of tunnel stiffness	11.6, 45.5	7.5, 12.5
Tunnel length: 57.5 m			

Regarding the tunnel, two different embedded tunnel depths were compared to investigate the effects of tunnel depth on tunnel responses to faulting. A summary of the numerical analysis of tunnel-faulting interaction is given in Table 2.3.

2.4 Interpretation of Three-Dimensional Centrifuge Tests and Numerical Simulations

The experimental and numerical results were analyzed to reveal the interaction between fault rupture and underground structures. Data presented here are converted into prototype scale, unless stated otherwise.

2.4.1 Ground Surface Settlements Adjacent to the Single Pile and Pile Group

Figure 2.7a compares the measured and computed ground surface settlements in the single pile test. Both the measured and computed results show that the ground surface on the footwall side remained stationary while that on the hanging wall side settled with the bedrock fault movement. Computed results further illustrate that the differential settlement mainly occurred at $-1.5\text{ m} < X < 3.5\text{ m}$, where X is the horizontal distance from the free-field rupture outcrop (see Figs. 2.1 and 2.6). For the smallest vertical fault movement of $h = 0.4$ m simulated, the differential settlement reveals an error function-type profile as suggested by Cai and Ng (2013):

$$d_Z = \left[1 + \text{erf}\left(\frac{X}{2.70} + 0.15\right)\right] \tag{2.2}$$

where d_Z is the ground surface settlement.

For the larger vertical movements (i.e., h larger than 0.4 m), a localized differential settlement and scarp were developed at the ground surface on the hanging wall side of the pile and the measured settlement profile could be fitted well with the error function qualitatively, although the settlement profile underestimated by the error function quantitatively (Cai and Ng 2016).

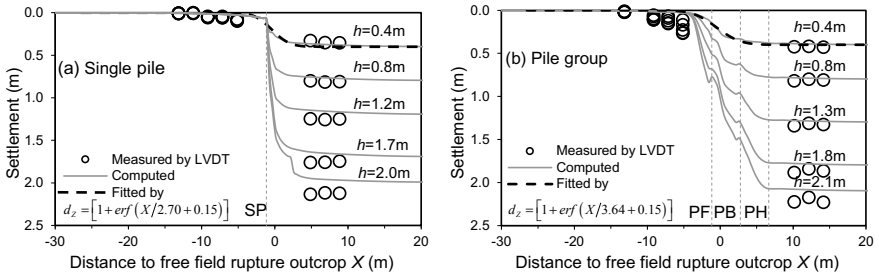

Fig. 2.7 Development of ground surface settlement induced by faulting from **a** the single pile test; **b** the pile group test

Figure 2.7b shows the ground surface settlement with the presence of a pile group. Compared with the differential settlement zone for the single pile, that for the pile group is extended by 2.5 times (i.e., -4 m $< X <$ 8.5 m). For the vertical fault movement of h = 0.4 m simulated, the differential settlement may be captured by an error function-type profile as follows:

$$d_Z = \left[1 + \mathrm{erf}\left(\frac{X}{3.64} + 0.15\right)\right] \tag{2.3}$$

No scarp was formed at the ground surface. In addition, a relatively small ground settlement was observed around pile PF, suggesting a relative displacement between the pile and the surrounding soil. For h larger than 0.4 m, the ground surface differential settlement further developed without formation of a scarp around the pile group (Cai and Ng 2016).

2.4.2 *Normal Fault Propagation in Sand and Fault-Pile Interaction*

Figure 2.8 compares the results of experiments and numerical simulations after faulting for a single pile (h = 2 m) and a pile group (h = 2.1 m). A fault rupture was found to have extended from the bedrock fault to the ground surface with a dip angle of 80° in the single pile test (see Fig. 2.8a). A scarp emerged on the hanging wall side of the pile. Figure 2.8b shows the computed plastic shear strain for the same test. The plastic shear strain was mainly induced near the fault rupture suggesting the fault rupture was of a shearing type. In addition, both the centrifuge and numerical results suggest that the fault rupture refracted (i.e., became steeper) at the soil–bedrock interface. The same phenomenon has also been observed in centrifuge tests conducted on free-field sand beds (Anastasopoulos et al. 2007) and was probably related to the more dilatant behavior of sand (Bray et al. 1994; Anastasopoulos et al. 2007).

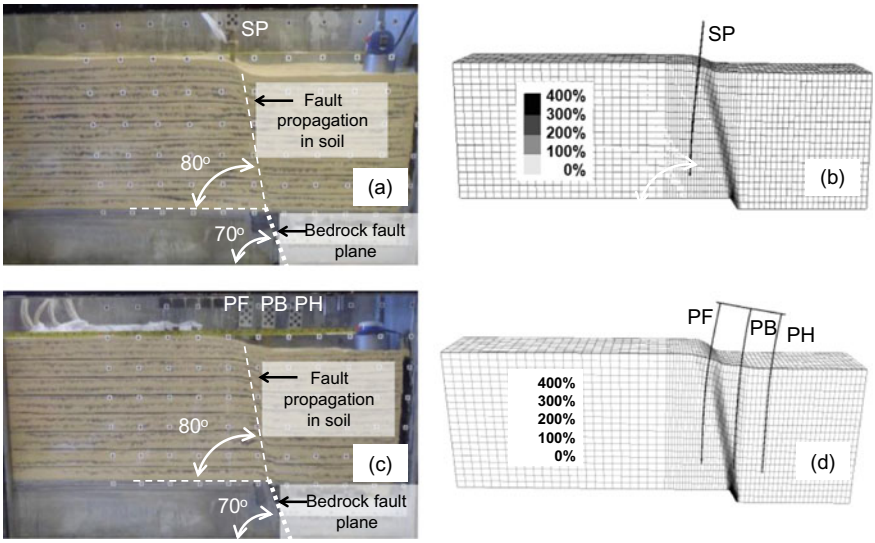

Fig. 2.8 Interaction between fault propagation and **a** the single pile from the centrifuge test; **b** the single pile from the numerical analysis; **c** the pile group from the centrifuge test; and **d** the pile group from the numerical analysis

Figure 2.8c shows the soil deformations after faulting for the pile group. The location of the induced fault rupture was similar to that observed for the single pile case. The fault rupture developed between the two piles PF and PB. As shown in Fig. 2.8d, the numerical back-analysis reveals that the fault rupture passed through the tip of pile PB and emerged at the ground surface on the footwall at the location of pile PF. Compared with the single pile case, the presence of two more piles (i.e., PB and PH) in the three-pile group did not alter the location and angle of the fault rupture, except the differential settlement zone was extended (as shown in Fig. 2.7b). In their numerical analyses of pile-fault interaction, Anastasopoulos et al. (2013) observed that the pile group altered the path of fault rupture. They found that the rupture passed through the tip of the piles and emerged at the ground surface when the pile group was positioned further away on the hanging wall side. While the main rupture zone was not affected, a secondary rupture was generated between the piles resulting in the modification of the fault rupture path. Generally, the observations from the centrifuge tests and numerical back-analyses were consistent, lending confidence to the other reported results.

2.4.3 Pile Top Displacement and Tilting

Figure 2.9a compares the measured and computed displacements at the single pile tip during five steps of faulting simulation. The measured and computed results are

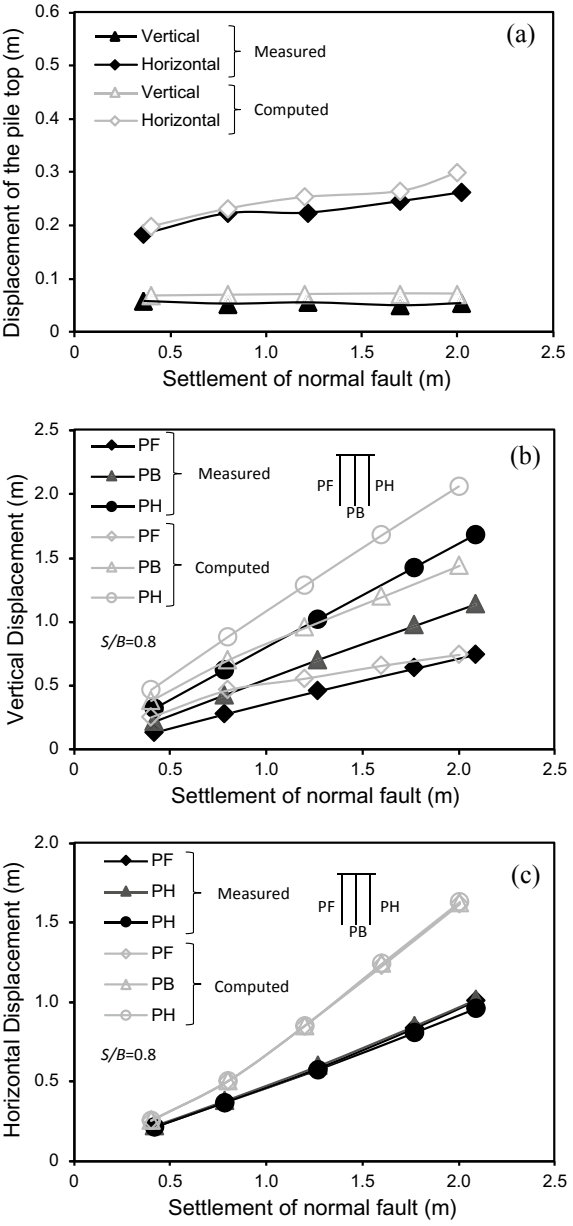

Fig. 2.9 Measured and computed **a** displacement of the single pile; **b** vertical displacement of the pile group; and **c** horizontal displacement of the pile group

fairly consistent with each other and revealed that the settlement of the single pile was induced during the first step of faulting (h = 0.4 m) with no further increase in the subsequent steps (i.e., h = 0.8, 1.3, 1.8 and 2.0 m). Most of the pile horizontal displacement was also observed during the first step of faulting but with a slight increase during the subsequent steps.

As illustrated in Fig. 2.9b, the measured vertical displacements of the three piles (PF, PB and PH) in the pile group varied linearly with the settlements of the hanging wall during the five steps of faulting simulation. The computed results show a consistent trend but with some overestimation. The linearly increasing difference among the measured settlements of the three piles reveals that the pile group tilted toward the hanging wall after each step of faulting. The same phenomenon was also observed in the numerical analyses of a 2 × 4 pile group conducted by Anastasopoulos et al. (2013). The PB and PH piles were pulled downwards and sideways due to the settlement of the hanging wall, whereas pile PF resisted on the footwall side. Consequently, the piles on the hanging wall side (PB and PH) experienced large bending moments at their heads.

Based on technical code for building pile foundations (JGJ 94-2008), the ultimate bending moment capacity of the 0.65 m diameter pile with the maximum design reinforcement ratio of 0.75% is 550 kN m. When h = 2.1 m, the computed maximum bending moments of piles for PF, PB and PH are 2,385 kN m, 2,859 kN m and 2,310 kN m, respectively. This means that the induced bending moments are at least four times larger than the ultimate design capacity. Regarding axial force induced in each pile, the computed maximum tensile force induced in pile PB is 1,212 kN, which exceeds the ultimate axial tension capacity of 771 kN and the pile will be damaged in a tensile-failure mode. Anastasopoulos and Gazetas (2007) reported tensile failure in piles due to normal faulting during the Kocaeli 1999 earthquake. The piles crossing the fault rupture failed under tension and the piles adjacent to the surface rupture showed tensile cracking. Hence, the induced tensile stress must be considered in any design analysis.

Figure 2.9c compares the measured and computed horizontal displacements of the three piles during faulting. The measured horizontal displacements increased linearly with the magnitude of faulting simulated and were almost identical suggesting a rigid body movement of the pile group in the horizontal direction. Similar results were also obtained from the numerical simulation. This implies that the three piles were well connected by the pile cap and displaced toward the hanging wall horizontally after faulting. The observed differences in the vertical displacements of the three piles (refer to Fig. 2.9b) must have been resisted by the bending moment of the pile cap. The induced maximum sagging bending moment in the pile cap was 6913 kN m, which exceeds 42% of its bending moment capacity. Consequently, an increase in the thickness and reinforcement ratio of the pile cap must be considered in the structural design (Anastasopoulos et al. 2013).

Due to displacements of the PB and PH piles, the pile cap was pulled and tilted towards the hanging wall after faulting. Based on the computed results, the pile PF resisted the faulting actions through an increase in axial compression of 1,057 kN (52% of axial compression capacity of 2,038 kN). Moreover, the computed horizontal displacements of the three piles were identical, and they also increased with the magnitude of faulting simulated. However, the differences in the computed and measured values increased with the magnitude of faulting, probably because the interface between each pile and its surrounding soil was not properly simulated numerically.

2.4.4 *Influence of Pile Location on Pile Responses: Numerical Parametric Study*

Based on the numerical parametric analyses, Fig. 2.10a illustrates the effects of the distance from the farthest face of single pile to the free-field fault outcrop (S) on pile displacement, when it was subjected to bedrock fault movement of h = 0.4 m. The S is normalized by the pile diameter. Based on the single pile response, three characteristic zones (I, II, III) may be identified. When the single pile was located on the footwall side and far from the bedrock fault (i.e., $S/D < -10$), no significant displacement or tilting was expected and hence the pile remained stationary after faulting. This is consistent with the results of centrifuge tests on single piles by Yao and Takemura (2020) who found that the piles out of the fault zone were practically unaffected by fault propagation. It may be defined as a safe zone (I) (i.e., $S/D < -10$) for any building to be constructed.

As the location of the single pile approached the bedrock fault line from $S/D = -10$ m onward, the horizontal displacement and tilting of the pile increased and reached their peak values when the pile reached $S/D = -0.8$ and then decreased to their respective, almost steady values at S/D = 5. These results agree well with Yao and Takemura's (2020) observation that the maximum horizontal displacement of the single pile would occur when the pile is located near the bedrock fault line where the normal fault rupture propagates through the single pile. On the other hand, the vertical displacement of the pile increased from $S/D = -10$ onward, almost linearly with S/D to reach a nearly steady value at S/D = 5. Thus, the normalized distance of $-10 < S/D < 5$ may be defined as the transition zone (II) in which special design considerations are likely to be needed.

When the single pile was located at a distance $S/D \geq 5$ on the hanging wall side, the pile displaced by almost the same amount as the hanging wall (i.e., h = 0.4 m), revealing a vertical rigid body movement together with its surrounding soil. On the other hand, the pile displaced horizontally by about 50% of the settlement but without any pile tilting. This implies that the pile simply translated

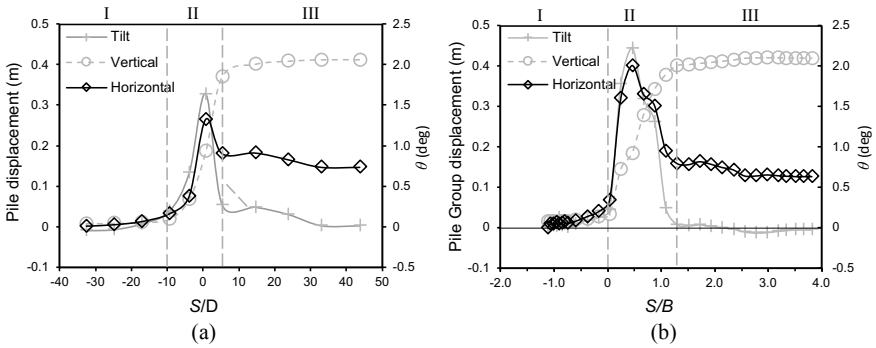

Fig. 2.10 Influence of pile location on the response of **a** single pile and **b** pile group

along a locus inclining at about 63.4° to the horizontal, as opposed to the dip angle of 80° observed in Fig. 2.8a. This zone may be defined as the translational zone (III) when $S/D \geq 5$. In this zone, the fault rupture could be accommodated by the rigid body movement of the structure (Oettle and Bray 2013).

Figure 2.10b shows the computed response of the 3 × 1 pile group to the faulting with a magnitude of 0.4 m for different distances (S) from the furthest edge of the pile group cap to the free-field fault rupture outcrop. Each S in the figure is normalized by the width B (i.e., 9.5 m in prototype) of the pile group cap (as defined in Fig. 2.1). Very similar responses to the single pile were computed, except the magnitudes were slightly different. Thus, the three characteristic zones can also be identified. Similar to the single pile case, $S/B < 0$ can be defined as the safe zone (I), and $0 < S/B < 1.3$ as the transition zone (II). The translational zone (III) occurs where $S/B \geq 1.3$. The peak vertical displacement of 0.4 m and the corresponding horizontal displacement of 0.15 resulted in a translational locus of about 69° to the horizontal, which was slightly steeper than that in the single pile case. Similar characteristic zones were also observed by Anastasopoulos et al. (2013) through numerical simulation of a 2 by 4 pile group subjected to normal fault propagation.

To further investigate the response and load redistribution of individual piles in the elevated pile group at different locations, Fig. 2.11 shows the computed axial forces (above the ground surface) of the three piles (PF, PB and PH) when h = 0.4 m. The same three characteristic zones can be easily identified as those based on pile group displacements shown in Fig. 2.10b. In zone I, the three piles share almost the same amount of applied working load of 1250 kN each. This zone may be called a safe zone (I) as shown in Fig. 2.10b.

In zone II ($0 < S/B < 1.3$), the middle pile PB behaves very differently to the other two piles PF and PH. The compressive force in PB increases to a maximum of 2853 kN which is 40% larger than the ultimate axial compressive capacity of

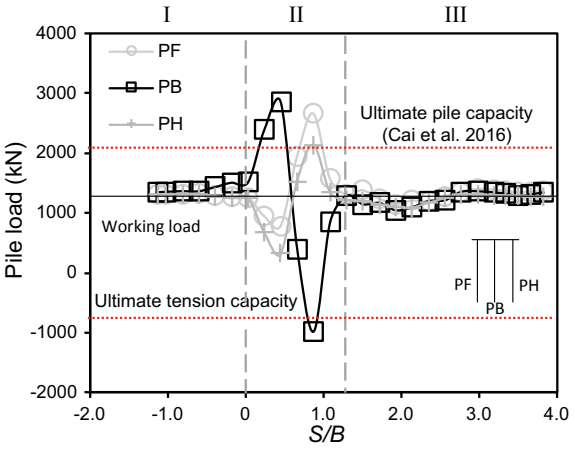

Fig. 2.11 Redistribution of axial forces within the pile group at different locations

2,038 kN. Obviously, this should be considered in any design analysis. On the contrary, the compressive axial forces in PF and PH decrease to their minimum values of 671 kN and 319 kN, respectively. Interestingly, a neutral point can be identified, i.e., $S/B = 0.6$, at which the three piles are all subjected to the same working load before faulting. When the pile cap is located at S/B larger than 0.6, the axial compressive force induced in pile PB decreases and reaches its largest tension of 986 kN at $S/B = 0.9$. This induced tension is 128% of the ultimate tension capacity (i.e., 771 kN) and the pile could be damaged in a tensile-failure mode. Hence, the induced tensile stress must be considered in any design analysis. In contrast, the axial compressive forces in PF and PH increase to their maximum values of 2,668 kN and 2,139 kN, respectively, to maintain the vertical force equilibrium. The axial force in both piles exceeds the ultimate axial compressive capacity and reach to 131 and 105% of its ultimate axial compressive capacity of 2,038 kN, respectively. As the pile group moves away from the fault line, the tensile force in PB and compressive forces in PF and PH all return to their initial working values at $S/B = 1.3$. Based on the computed results, one may define $0 < S/B < 1.3$ as the transition zone (II) in which the axial force is significantly redistributed among the three piles. Within this zone, it is fairly clear that a minimum of 131% of the ultimate axial compressive capacity should be considered for all three piles. On the other hand, a minimum tensile capacity of about 986 kN should be allowed for pile PB. When the pile group is located at $S/B \geq 1.3$, no redistribution of the axial forces among the three piles can be found. This is consistent with the translational zone (III) identified in Fig. 2.10b.

Figure 2.12 shows the effects of pile group location on the response of the pile group subjected to different levels of normal fault movement from numerical simulations. When the pile group is located on the footwall side and far from the bedrock fault (i.e., zone I with $S/B < 0$), no significant displacement and tilting are observed and hence the pile cap remained stationary after faulting. In this zone, the induced tilting of the pile cap is within the allowable tilting limit of 0.11° (i.e., 0.2%) suggested by Eurocode 7 (CEN 2001) for buildings.

In zone II ($0 < S/B < 1.3$), the horizontal displacement progressively increases while the vertical displacement and tilting reach their peak values following a subsequent decrease as the pile group approaches at $S/B = 1.3$. The rotation (or tilting) of the pile cap increases with the normal fault settlement within this zone. Irrespective of the level of normal fault settlement in zone II, the tilting of the pile cap exceeds the allowable tilting limit of buildings suggested by Eurocode 7 (CEN 2001). In zone III, the vertical and horizontal displacements and hence the tilting of the pile group reach their ultimate values. Similar to zone I, the induced tilting of the pile cap by the five levels of normal fault movements is within the allowable tilting limit suggested by Eurocode 7 (CEN 2001). This suggests that the tilting remains constant (i.e., close to zero) in zones I and III and hence the range of the three identified zones for pile group location is not affected by the magnitude of the normal fault movement. Similar behavior was observed by Anastasopoulos et al.

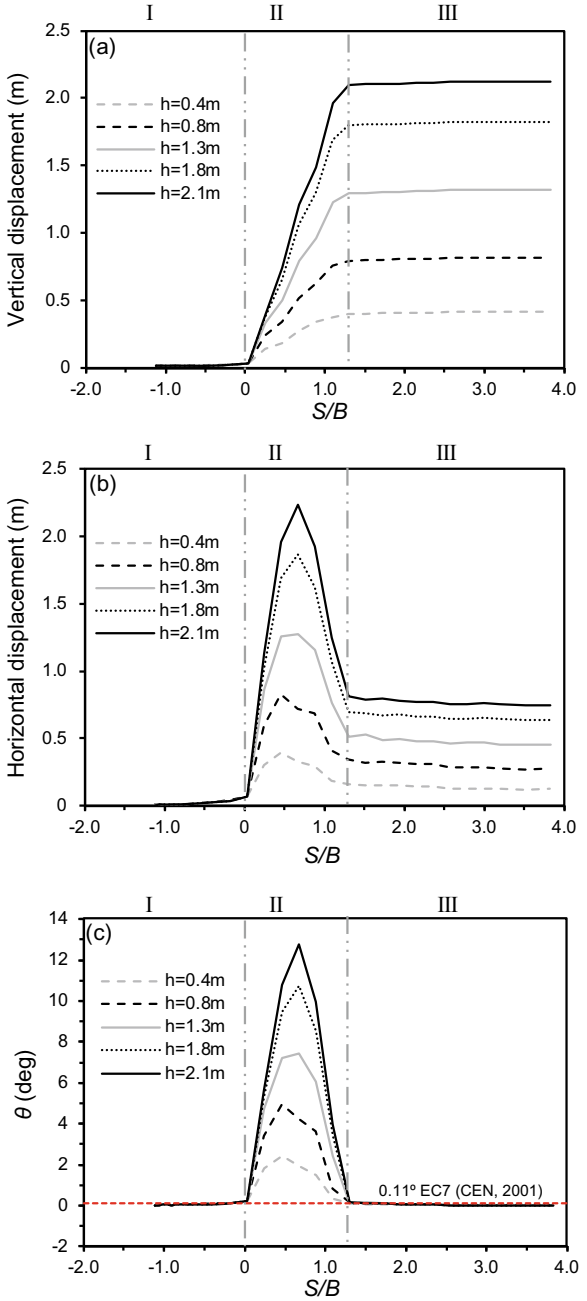

Fig. 2.12 Effects of normalized distance from pile group to fault rupture on the computed: **a** vertical displacement; **b** horizontal displacement; and **c** tilting of the pile group

(2013) for a 2 × 4 pile group suggesting the effectiveness of the chosen distance normalization (i.e., S/B) for identifying the three characteristic zones.

Figure 2.13 shows the effects of pile group location on the computed maximum and minimum bending moments induced in piles PF, PB and PH subjected to the five levels of normal fault movements. The induced bending moments in the figure are normalized by the ultimate bending capacity of the piles. The ultimate moment capacity of the pile with a diameter of 0.65 m and the maximum design reinforcement ratio of 0.75% (based on Technical code for building pile foundations (JGJ 94-2008)) is 550 kN m. In zone I ($S/B < 0$), the piles remain at the footwall sustaining (relatively) limited distortion since the propagating fault rupture has not passed through the piles (see Fig. 2.12c). Hence, the bending moments of the piles remain almost zero. As the fault rupture hits the piles in zone II, the pile group acts as a retaining system of the soil mass behind the piles resulting in an increase in their tilting (see Figs. 2.8 and 2.12) and bending moments. The tilting and the associated bending moments reach their peak values in zone II. For a normal fault settlement of 0.4 m, the bending moments of piles PF, PH and PB reach 152%, 130% and 160% of their bending capacity, respectively. Furthermore, the induced maximum sagging bending moment in the pile cap reach to 4401 kN m, which is 90% of its bending capacity. The maximum induced moment in the piles increase with settlements of the normal fault. For the normal fault settlement of 2.1 m, the bending moments of piles PF, PH, and PB reach 430%, 550% and 580% of their bending capacity, respectively. Similar observations were reported by Anastasopoulos et al. (2013) suggesting that special design considerations such as increases in the reinforcement and pile diameter are likely to be needed for the piles in this zone. The induced maximum sagging bending moment in the pile cap reach to 6913 kN m, which is 140% of its bending capacity. Consequently, an increase in the thickness and reinforcement ratio is required during the structural design of the pile cap (Anastasopoulos et al. 2013).

As the fault rupture passes beyond the pile cap in zone III ($S/B > 1.3$), the pile group follows the movements of the hanging wall in its downward and outward translational directions, and hence, the induced bending moments are smaller than the bending capacity of the piles. Based on the results revealed in Figs. 2.10, 2.11, 2.12, 2.13, it is reasonable to define the three characteristic zones, i.e., safe, transition and translational, for design analyses.

2.4.5 *Ground Surface Settlement Along the Longitudinal and Transverse Tunnel Directions*

Figure 2.14 compares measured and computed ground surface settlement profiles along the tunnel axis with a fault magnitude of $h = 0.8$ m. The computed vertical displacements of the tunnel crown are also given in the figure for comparison. As illustrated in Fig. 2.14a, the measured ground surface settlement above the tunnel

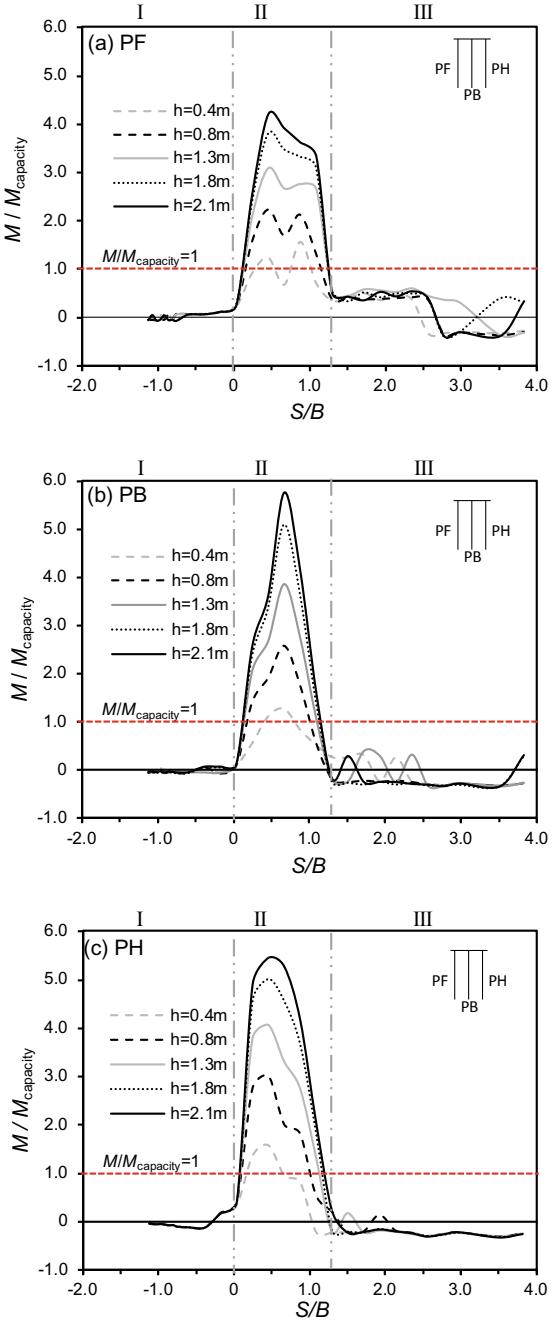

Fig. 2.13 Effects of distance from pile group to fault rupture on the computed bending moment of pile **a** PF; **b** PB; and **c** PH

with a tunnel depth (d_T) of 7.5 m increases gradually from the footwall side to the hanging wall side, resulting in an average ground surface gradient of 2.1%, which is consistent with the computed results of about 2.0%. Similarly, the average computed tunnel crown settlement gradient is 2.0% which far exceeds the recommended serviceability limit of 0.1% for a tunnel by the Land Transport Authority (LTA 2000) in Singapore, as expected. It is also found that computed settlements at the tunnel crown for $X > -17.5$ m far exceed the recommended serviceability limit of 15 mm by the Land Transport Authority (LTA 2000), as expected. Figure 2.14b compares measured and computed ground surface settlement profiles above the tunnel when it is located at a depth of 12.5 m after the same fault movement. There is no major difference between the measured and computed results when the tunnel is located at either 7.5 m or 12.5 m. The measured ground settlement profile is consistent with the computed ground surface profile and with tunnel crown settlements with an average slope of 2.2%, except when X is greater than 0 from the free-field fault rupture outcrop. Similar to the tunnel located at a depth of 7.5 m, the average computed slope of the tunnel crown settlement far exceeds the limit of 0.1% (LTA 2000). The increasing discrepancy between measured and computed ground surface profiles when $X > 0$ may be attributed to the continuum assumption made in the numerical simulations, opposite to the particulate behavior of model sand used in the experiments, especially near the fault line. Furthermore, the settlements at the tunnel crown for $X > -19$ m exceed the recommended serviceability limit of 15 mm by (LTA 2000), irrespective of the tunnel depth. All these results suggest that special design consideration should be given for tunnel located nearby a fault zone.

Figure 2.15 compares measured and computed ground surface settlements perpendicular to the longitudinal tunnel axis when the fault magnitude is $h = 0.8$ m. To investigate the stiffening effects provided by the tunnel, three different magnitudes of tunnel stiffness (i.e., $E_TI = 4.71 \times 10^8$ kN m^2, $0.65E_TI = 3.06 \times 10^8$ kN m^2 and $0.17E_TI = 0.80 \times 10^8$ kN m^2) are considered in the numerical analyses. Comparing the computed results of three different tunnel stiffness, it is found that there is no major difference in the computed soil settlement profiles. When the tunnel is located at 7.5 m deep (Fig. 2.15a), the measured induced

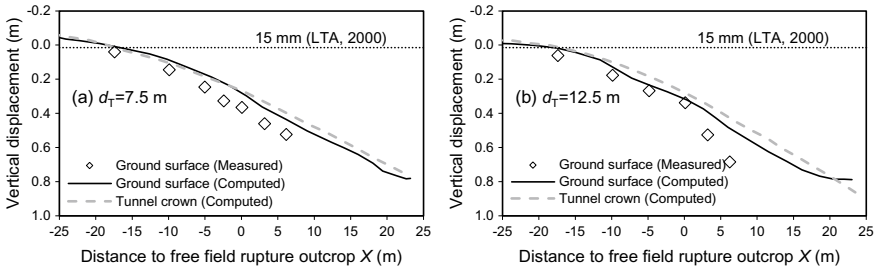

Fig. 2.14 Development of ground surface settlement induced by faulting with the tunnel axis at **a** $d_T = 7.5$ m; and **b** $d_T = 12.5$ m

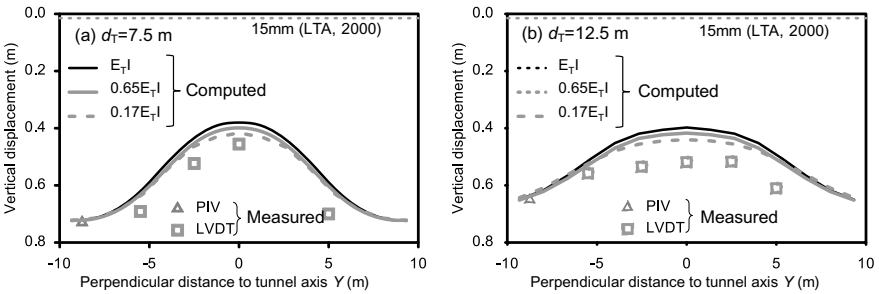

Fig. 2.15 Development of ground surface settlements induced by faulting (h = 0.8 m) perpendicular to the longitudinal tunnel axis with tunnel depth located at **a** d_T = 7.5 m; and **b** d_T = 12.5 m

settlement of the ground surface above the tunnel axis (at Y = 0 m) is 0.45 m, which reveals that the soil above the tunnel experiences a settlement far exceeding the allowable limit of 15 mm recommended by LTA (2000) in Singapore. The ground surface settlement displays an inverted U shape profile, where the minimum settlement occurs at the location of the tunnel. As expected, the shielding effects of the tunnel are the highest near the tunnel axis, and it decreases with an increase of the distance from its longitudinal axis. The measured ground surface settlement reaches the maximum value of 0.72 m at Y = −8.75 and 8.75 m. Although the measured surface settlements are underestimated slightly by the numerical analyses, the computed results are generally in good agreement with the measurements.

Figure 2.15b compares measured and computed ground surface settlement profiles induced by faulting perpendicular to the longitudinal tunnel axis when the tunnel is located at a depth of 12.5 m. The measured soil settlement profile similar to that of the tunnel located at 7.5 m is observed, except that the increase in the burial depth of the tunnel results in a slight increase in ground surface settlement (i.e., the settlement increases to 0.50 m at Y = 0 m). Similar to the tunnel at a depth of 7.5 m, the ground surface settlement exceeds the allowable limit of 15 mm recommended by LTA (2000). The ground surface settlement profile shows a similar inverted U shape profile to the tunnel depth at a depth of 7.5 m, except the settlement profile spreads wider with an increase in the tunnel depth. Consequently, the maximum ground surface settlement is smaller for the deeper tunnel, and it reaches 0.65 m at Y = −8.75 and 8.75 m. The observed wider settlement profile of the deeper tunnel near the bedrock is consistent with the results of Baziar et al. (2014) who conducted a series of centrifuge tests on a tunnel subjected to reverse faulting. They found that an increase in the tunnel depth can cause the rupture to be modified near the tunnel and propagate in a wider zone of soil layer above the tunnel.

2.4.6 *Propagation of Normal Fault and Fault-Tunnel Interaction*

Figure 2.16a shows the computed plastic shear strain contours when the tunnel is located at d_T = 7.5 m. While the hanging wall block moved at an angle of 70° with respect to the horizontal, the fault rupture in the soil underneath the tunnel extends upward with a dip angle of 80°, similar to the sand bed strengthened by the presence of the single pile and the pile group (refer to Fig. 2.8). An increase in the dip angle of fault rupture from 70° in bedrock to 80° in soil is probably related to the dilatant behavior of sand. The same phenomenon has also been observed in centrifuge tests conducted on free-field sand beds (Anastasopoulos et al. 2007). For the soil above the tunnel, no fault rupture can be observed. This suggests that the soil above the tunnel is shielded from the shearing deformation arising from faulting. When the tunnel is located at d_T = 12.5 m, a similar propagation of fault rupture is computed as shown in Fig. 2.16b. The fault rupture is shielded from propagating upward after reaching the tunnel. The shielding effects of the embedded tunnel have also been observed by Baziar et al. (2014) in centrifuge tests in which the tunnel axis was parallel to the bedrock fault plane. In their study, a scarp emerged at the ground surface since the fault rupture might have bypassed the tunnel and the extent of shielding depended on the horizontal tunnel distance from the fault rupture. However, the shielding effect of the tunnel is more apparent when the tunnel is perpendicular to the bedrock fault plane and no scarp could emerge at the ground surface due to the stiffening effects of the tunnel.

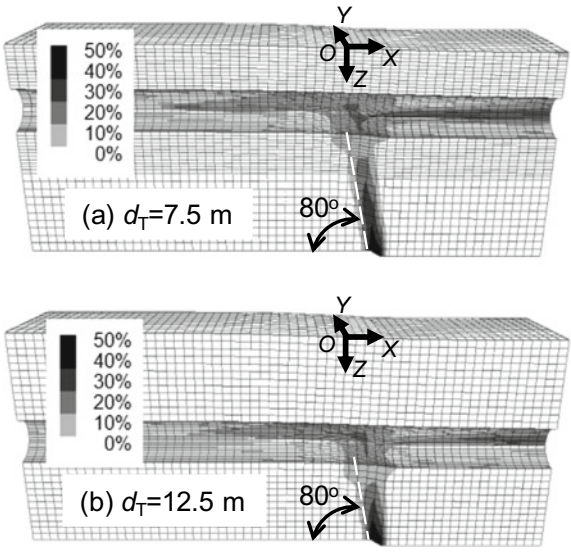

Fig. 2.16 Computed plastic shear strain contours due to fault propagation when the tunnel is located at **a** d_T = 7.5 m; and **b** d_T = 12.5 m

Figure 2.17 compares the measured and computed additional longitudinal tensile strains induced at the tunnel crown after faulting with a magnitude of h = 0.8 m. The measured values and computed results are in excellent agreement. The distributions of the longitudinal strains at the tunnel crown show that the tunnel was subjected to a hogging moment after normal faulting. Tensile strains were induced at the tunnel crown and the peak tensile strain was located near the middle of the model tunnel (i.e., X = −6.5 m) in both centrifuge tests. The measured peak tensile strains were 1,697 $\mu\varepsilon$ and 2,566 $\mu\varepsilon$ when the tunnel was located at the depths of 7.5 m and 12.5 m, respectively. The measured tensile strain decreased to zero toward the two free ends of each tunnel.

By comparing the results of strains induced in the tunnels located at the depths of 7.5 and 12.5 m, it is clear that the maximum induced tensile strain (i.e., 2,566 $\mu\varepsilon$) at d_T = 12.5 m is about 50% larger than that (i.e., 1,697 $\mu\varepsilon$) at d_T = 7.5 m. This is because the extent of the hogging deformation of the tunnel increased with burial depth. The part of the tunnel exceeding the limiting cracking tensile strain of 150 $\mu\varepsilon$ for unreinforced concrete (ACI 2001) is located at −29.5 m < X < 16.5 m and −35.0 m < X < 13.0 m when the tunnel is 7.5 m and 12.5 m deep, respectively. In other words, the length of excessive tensile zone is 46 m and 48 m for d_T equals to 7.5 m and 12.5 m, respectively. This implies that sufficient reinforcements must be provided to limit tensile cracking to an acceptable level in a fault zone. Based on centrifuge tests, similar results were reported by Baziar et al. (2014) suggesting that a deeper tunnel near the bedrock fault requires larger flexibility to prevent cracking due to fault movement. An alternative design method is to set flexible joints to accommodate deformation due to rupturing for the tunnels crossing an active fault (Kiani et al. 2016).

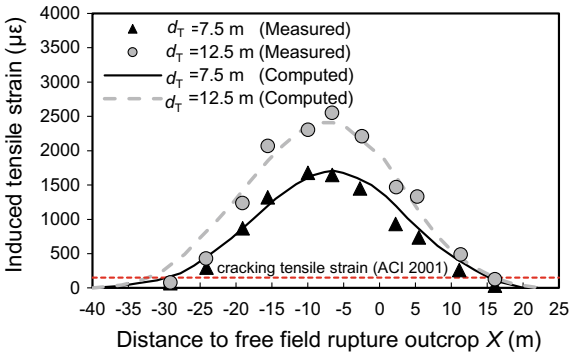

Fig. 2.17 Longitudinal tensile strains induced at the tunnel crown (h = 0.8 m)

2.5 Summary and Conclusion

Based on a series of centrifuge model tests and numerical analyses on pile foundations and tunnel subjected to normal faulting, the following conclusions may be drawn.

For a single pile located on the footwall, both measured and computed vertical displacements of the pile are consistent, and they are independent of the four levels of faulting movement simulated. On the other hand, the horizontal displacement of the pile increases almost linearly with the magnitude of the faulting induced. Three characteristic zones may be identified: (1) safe zone—I (i.e., $S/D \leq -10$), where no significant displacement or tilting is expected and hence the pile remains stationary after faulting; (2) transition zone—II (i.e., $-10 < S/D < 5$) where the pile is displaced and tilted toward the hanging wall and hence special design considerations are needed; and (3) translational zone—III (i.e., $S/D \geq 5$), where the pile is displaced translationally but without tilting.

Similarly, three characteristic zones, i.e., safe zone I ($S/B \leq 0$), transition zone II ($0 < S/B < 1.3$) and translational zone—III ($S/B \geq 1.3$), can also be identified for pile groups. The range of the three identified zones is not affected by the magnitude of the normal fault movements simulated.

For the pile group located at $S/B = 0.8$ in the transition zone—II ($0 < S/B < 1.3$), the piles on the hanging wall side (PB and PH) are pulled downward and sideways due to the settlement of the hanging wall, whereas pile PF resisted on the footwall side. With a fault movement of $h = 2.1$ m, for an example, the computed maximum bending moments of piles PF, PB and PH are 2,385 kN m, 2,859 kN m and 2,310 kN m, respectively, as compared with the ultimate moment capacity of 550 kN m. The computed maximum tensile force induced in pile PB is 1,212 kN which exceeds the ultimate tension capacity of 771 kN by 57% and the pile will be damaged in a tensile-failure mode. Hence, the induced bending moment and tensile stress must be considered for designs.

In the transition zone, the middle pile PB behaves very differently to the other two piles PF and PH. For example, when $h = 0.4$ m, the compressive axial force in PB increases with S/B and reaches the maximum of 2,853 kN which exceeds 40% of its ultimate axial compressive capacity. However, the axial force induced in pile PB decreases when the pile group is located at $S/B = 0.9$ and the largest induced tension in pile PB reaches 986 kN, which is 28% larger than its tension capacity. This implies that the performance of the middle pile is mostly affected by the location of pile group.

The tilting of the pile cap and the associated bending moments increase with the magnitude of normal fault settlement within the transition zone II ($0 < S/B < 1.3$), whereas the tilting remains constant (i.e., close to zero) in zones I and III, irrespective of the magnitude of fault settlement. In zone II, the tilting of the pile cap far exceeds the allowable tilting limit of buildings suggested by Eurocode 7 (CEN 2001). The tilting and the associated bending moments reach their peak values in this zone. As expected, the maximum induced moment in the piles increases with

the magnitude of fault settlements. During the normal fault settlement of 2.1 m, for example, the bending moments of piles PF, PH, and PB reach 430%, 550% and 580% of their bending moment capacity, respectively. The maximum sagging bending moment induced in the pile cap reaches 6,913 kN m, which is 142% of its bending moment capacity. Consequently, an increase in thickness and reinforcement in pile cap should be considered. In the translational zone III ($S/B \geq 1.3$), the pile group follows the movements of the hanging wall in its downward and outward translational directions and hence the induced bending moments are smaller than the bending moment capacity of the piles.

When there is a tunnel constructed in sand stratum, the ground above the longitudinal axis of the tunnel is shielded from the shearing deformation due to faulting. As expected, the gradient of induced tunnel crown settlement far exceeds the recommended serviceability limit of 0.1% for a tunnel by the Land Transport Authority (LTA 2000) for both tunnels at depths of 7.5 and 12.5 m. Perpendicularly to the longitudinal tunnel axis (i.e., transverse direction), the ground surface settlement reveals an inverted *U* shape profile. This suggests that the shielding effects of the tunnel are higher near the longitudinal tunnel axis and it decreases with an increase of the distance from the tunnel axis. Due to the 0.8 m faulting, for example, the tunnel is subjected to a hogging bending moment and longitudinal tensile strain is induced at the tunnel crown. When the tunnel depth d_T increases from 7.5 to 12.5 m, the maximum induced tensile strains increase by about 50%. The length of the tunnel exceeding the limiting cracking tensile strain of 150 $\mu\varepsilon$ for unreinforced concrete (ACI 2001) also increases slightly with the tunnel depth. For the cases investigated, the length of the excessive tensile zone is 46 m and 48 m for d_T equals to 7.5 m and 12.5 m, respectively. This implies that sufficient reinforcement should be provided.

Acknowledgements The authors would like to acknowledge the financial support provided by the National Natural Science Foundation of China (grant nos. 51778249 and 51608170), the Natural Science Foundation of Fujian Province of China (project no. 2018J01072), the Promotion Program for Young and Middle-aged Teachers in Science and Technology Research of Huaqiao University (project no. ZQN-PY216), and Huaqiao University (project no. 16BS509).

References

ACI (American Concrete Institute) (2001) Control of cracking in concrete structures. ACI 224R-01. Farmington Hills, MI

ACI (American Concrete Institute) (2011) Building code requirements for structural concrete and commentary. ACI 318M-11. Farmington Hills, MI

Ahmed W, Bransby MF (2009) Interaction of shallow foundations with reverse faults. J Geotech Geoenviron Eng ASCE 135(7):914–924

Anastasopoulos I, Gazetas G (2007) Foundation-structure systems over a rupturing normal fault: part I. Observations after the Kocaeli 1999 earthquake. Bull Earthq Eng 5(3):253–275

Anastasopoulos I, Gazetas G, Bransby MF, Davies MCR, El Nahas A (2007) Fault rupture propagation through sand: finite-element analysis and validation through centrifuge experiments. J Geotech Geoenviron Eng ASCE 133(8):943–958

Anastasopoulos I, Callerio A, Bransby MF, Davies MCR, El Nahas A, Faccioli E, Gazetas G, Masella A, Paolucci R, Pecker A, Rossignol E (2008) Numerical analyses of fault-foundation interaction. Bull Earthq Eng 6(4):645–675

Anastasopoulos I, Gazetas G, Bransby MF, Davies MCR, El Nahas A (2009) Normal fault rupture interaction with strip foundations. J Geotech Geoenviron Eng ASCE 135(3):359–370

Anastasopoulos I, Kourkoulis R, Gazetas G, Tsatsis A (2013) Interaction of piled foundation with rupturing normal fault. Geotechnique 63(12):1042–1059

Ashtiani M, Ghalandarzadeh A, Towhata I (2015) Centrifuge modeling of shallow embedded foundations subjected to reverse fault rupture. Can Geotech J 77(2):558–566

Baziar MH, Nabizadeh A, Lee CJ, Hung WY (2014) Centrifuge modeling of interaction between reverse faulting and tunnel. Soil Dyn Earthq Eng 65:151–164

Baziar MH, Nabizadeh A, Khalafian N, Lee CJ, Hung WY (2019) Evaluation of reverse faulting effects on the mechanical response of tunnel lining using centrifuge tests and numerical analysis. Géotechnique (in press)

Bray JD, Seed RB, Cluff LS, Seed HB (1994) Earthquake fault rupture propagation through soil. J Geotech Eng 120(3):543–561

Cai QP, Ng CWW (2013) Analytical approach for estimating ground deformation profile induced by normal faulting in undrained clay. Can Geotech J 50(4):413–422

Cai QP, Ng CWW (2014) Effects of the tip depth of a pre-existing fracture on surface fault ruptures in cemented clay. Comput Geotech 56:181–190

Cai QP, Ng CWW (2016) Centrifuge modeling of pile-sand interaction induced by normal faulting. J Geotech Geoenviron Eng ASCE 142(10):04016046

Cai QP, Ng CWW, Luo GY, Hu P (2013) Influences of pre-existing fracture on ground deformation induced by normal faulting in mixed ground conditions. J Cent S Univ 20(2):501–509

Cai Q, Ng CWW, Hu P (2015) Boundary effects on ground surface rupture induced by normal faulting. Géotechnique Lett 5(3):161–166

Cai QP, Ng CWW, Chen XX, Guo LQ (2017) Failure mechanism and setback distance of single pile subjected to normal faulting. Chin J Geotech Eng 39(4):720–726 (in Chinese)

Cai QP, Peng JM, Ng CWW, Shi JW, Chen XX (2019) Centrifuge and numerical modelling of tunnel intersected by normal fault rupture in sand. Comput Geotech 111:137–146

CEN (2001) Eurocode 7, part 1: geotechnical design: general rules, final draft prEN 1997-1. European Committee for Standardization (CEN), Brussels, Belgium

Cole DA Jr, Lade PV (1984) Influence zones in alluvium over dip-slip faults. J Geotech Eng 110(5):599–615

Dong JJ, Wang CD, Lee CT, Liao JJ, Pan YW (2003) The influence of surface ruptures on building damage in the 1999 Chi-Chi earthquake: a case study in Fengyuan city. Eng Geol 71(1–2):157–179

EAK: Greek Seismic Code, Organization of Seismic Planning and Protection, Athens (2000) (in Greek)

EC8 (2002) Eurocode 8: design of structures for earthquake resistance. European Committee for Standardization (CEN)

Faccioli E, Anastasopoulos I, Gazetas G, Callerio A, Paolucci R (2008) Fault rupture-foundation interaction: selected case histories. Bull Earthq Eng 6(4):557–583

GB50011-2010 (2010) Code for seismic design of buildings. China Building Industry Press, Beijing (in Chinese)

Ishihara K (1993) Liquefaction and flow failure during earthquakes. Geotechnique 43(3):351–415

Itasca FLAC (2000) Fast lagrangian analysis of continua. Itasca Consulting Group Inc., Minneapolis

JGJ 94-2008 (2008) China Academy of Building Research (CABR), Technical code for building pile foundations, Ministry of Construction, China.

Kiani M, Akhlaghi T, Ghalandarzadeh A (2016) Experimental modeling of segmental shallow tunnels in alluvial affected by normal faults. Tunnel Undergr Space Technol 51:108–119

Land Transport Authority (LTA) (2000) Code of practice for railway protection. Development and Building Control Department, Singapore

Li TB (2008) Failure characteristics and influence factor analysis of mountain tunnels in epicenter zones of great Wenchuan earthquake. J Eng Geol 16(3):742–750 (in Chinese)
Loukidis D, Bouckovalas GD, Papadimitriou AG (2009) Analysis of fault rupture propagation through uniform soil cover. Soil Dyn Earthq Eng 29(11–12):1389–1404
Ng CWW (2014) The 6th ZENG Guo-Xi lecture: the state-of-the-art centrifuge modelling of geotechnical problems at HKUST. J Zhejiang Univ Sci A (Appl Phys Eng) 15(1):1–21
Ng CWW, Lu H (2014) Effects of the construction sequence of twin tunnels at different depths on an existing pile. Can Geotech J 51(2):173–183
Ng CWW, Van Laak PA, Tang WH, Li XS, Zhang LM (2001) The Hong Kong geotechnical centrifuge. In: Lee CF, Lau CK, Ng CWW, Kwong AKL, Pang PLR, Yin JH, Yue ZQ (eds) 3rd international conference soft soil engineering. Swets & Zeitlinger, Hong Kong, pp 225–230
Ng CWW, Van Laak PA, Zhang LM, Tang WH, Zong GH, Wang ZL, Xu GM, Liu SH (2002) Development of a four-axis robotic manipulator for centrifuge modeling at HKUST. In: Proceedings international conference physical modelling in geotechnics, St. John's Newfoundland, Canada, pp 71–76
Ng CWW, Li XS, Van Laak PA, Hou DYJ (2004) Centrifuge modeling of loose fill embankment subjected to uni-axial and bi-axial earthquakes. Soil Dyn Earthq Eng 24(4):305–318
Ng CWW, Cai QP, Hu P (2012) Centrifuge and numerical modeling of fault rupture propagation in clay with and without a pre-existing fracture. J Geotech Geoenviron Eng ASCE 138(12): 1492–1502
Ng CWW, Lu H, Peng SY (2013) Three-dimensional centrifuge modelling of the effects of twin tunnelling on an existing pile. Tunn Undergr Space Technol 35:189–199
Ng CWW, Soomro MA, Hong Y (2014) Three-dimensional centrifuge modelling of pile group responses to side-by-side twin tunnelling. Tunn Undergr Space Technol 43:350–361
Ng CWW, Hong Y, Soomro MA (2015) Effects of piggyback twin tunnelling on a pile group: three-dimensional centrifuge and numerical modelling. Géotechnique 65(1):38–51
Ng CWW, Wei J, Poulos HG, Liu HL (2017) Effects of multi-propped excavation on an adjacent floating pile. J Geotech Geoenviron Eng ASCE 143(7):04017021
Oettle NK, Bray JD (2013) Geotechnical mitigation strategies for earthquake surface fault rupture. J Geotech Geoenviron Eng ASCE 139(11):1864–1874
Taylor RN (1995) Geotechnical centrifuge technology. Blackie Academic and Professional, London
Wang WL, Wang TT, Su JJ, Lin CH, Seng CR, Huang TH (2001) Assessment of damage in mountain tunnels due to the Taiwan Chi-Chi earthquake. Tunn Undergr Space Technol 16(3): 133–150
Wang ZZ, Gao B, Jiang Y, Yuan S (2009) Investigation and assessment on mountain tunnels and geotechnical damage after the Wenchuan earthquake. Sci China Ser E Technol Sci 52(2): 546–558
White DJ, Take WA, Bolton MD (2003) Soil deformation measurement using particle image velocimetry (PIV) and photogrammetry. Geotechnique 53(7):619–631
Yao C, Takemura J (2020) Centrifuge modeling of single piles in sand subjected to dip-slip faulting. J Geotech Geoenviron Eng 146(3):04020001